



TITLE:

# Loss Control with Annealing and Lattice Kerker Effect in Silicon Metasurfaces

AUTHOR(S):

Liu, Libei; Zhang, Feifei; Murai, Shunsuke; Tanaka, Katsuhisa

---

CITATION:

Liu, Libei ...[et al]. Loss Control with Annealing and Lattice Kerker Effect in Silicon Metasurfaces. *Advanced Photonics Research* 2022, 3(3): 2100235.

ISSUE DATE:

2022-03

URL:

<http://hdl.handle.net/2433/278384>

RIGHT:

© 2021 The Authors. *Advanced Photonics Research* published by Wiley-VCH GmbH; This is an open access article under the terms of the Creative Commons Attribution License, which permits use, distribution and reproduction in any medium, provided the original work is properly cited.

# Loss Control with Annealing and Lattice Kerker Effect in Silicon Metasurfaces

Libei Liu, Feifei Zhang, Shunsuke Murai,\* and Katsuhisa Tanaka

The resonant phenomena of metasurfaces highly depend on the scattering strength of each component and their interferences. The losses modify the phase and reduce the amplitude of all multipoles; thus, the loss control is vital for obtaining the designed properties. Amorphous (*a*-)Si has a higher absorption coefficient than that of the crystalline form, which limits its optical application. A simple rapid thermal annealing (RTA) path to refine the *a*-Si metasurfaces is found. It is applied to the sputtering-made *a*-Si metasurface comprising square array of nanodisks. While the large loss smears out the resonances for the as-made metasurface, the sharp and near-zero reflectance with near-perfect absorptance is achieved after RTA, satisfying the lattice Kerker condition via the interference of magnetic and electric dipoles. At the lattice Kerker condition, the forward-enhanced and backward-reduced directional photoluminescence is observed from the emitter layer deposited on the metasurface. The numerical results are all found to be in good agreement with the experimental results, and the multipole expansion analysis for the single nanodisk gives the physical background of this observation. This refinement of *a*-Si metasurfaces by RTA treatment paves the simple and robust way for realizing thrilling optical and optoelectrical applications, such as detectors and filters.

## 1. Introduction


The manipulation of light field at nanoscale has been widely resorted to the metallic nanoparticles (NPs) in the past two decades.<sup>[1]</sup> The wide appeal of metallic NPs depends on its collective oscillation of free electrons or surface plasmons, which results in a strongly localized electromagnetic field in the vicinity of metallic NPs. However, the major hurdle that hinders the applications of metallic NPs is the intrinsic loss of metal and plasmonic resonance (the energy transfer from light fields to the kinetic energy

of free electrons always brings some losses).<sup>[2]</sup> Therefore, recent advances in nanophotonics have witnessed the emergence of dielectric NPs of high refractive indices with a low loss.<sup>[3–5]</sup> Contrary to the metallic NPs, both electric and magnetic modes exist in the dielectric resonators, showing a novel optical phenomenon and unique functionalities by tuning the electric dipole (ED) and magnetic dipole (MD) resonances (known as Mie resonances<sup>[6]</sup>), through tailoring the geometry and the spatial distributions of the individual resonators. The spectral overlap of ED and MD with equal intensities generates a scattering directionality, the so-called Kerker effect.<sup>[7]</sup> Precisely, the first Kerker condition brings zero-backward scattering, while the second condition results in zero-forward scattering.<sup>[8,9]</sup> When such NPs are placed into a periodic array, the periodicity of the lattice gives extra freedom in designing the transmittance/reflectance/absorptance. The radiative coupling of the dipoles in periodic

arrays is mediated by in-plane diffraction, leading to collective Mie scattering resonances or Mie surface lattice resonances (SLRs).<sup>[10]</sup> Further, the interference between ED and MD via SLR results in the lattice Kerker effect with zero transmittance/reflectance and perfect absorptance. Such optically functional metasurfaces are referred as Huygens' metasurfaces.<sup>[11]</sup>

Silicon is a representative dielectric material used for the ingredient of metasurfaces because of its high refractive index and established nanofabrication techniques that have been developed in the fields of electronics and semiconductor devices. There are several standard techniques to grow Si films for metasurface, and the final optical performance of the metasurfaces critically depends on the film quality. The most sophisticated technique is chemical vapor depositions (CVDs), which are based on thermal or plasma decomposition of SiH<sub>4</sub> gas. Crystalline (*c*-) Si and amorphous (*a*-) Si can be prepared with this process and applied to (opto)electric devices such as solar cells. The Si film can also be prepared from bulk Si targets using sputtering and electron beam deposition techniques. It is a very easy route compared with CVD involving toxic SiH<sub>4</sub> gas, but the film quality is generally low, that is, the film is amorphous and contains many defects. The film is highly absorptive, which smears out the resonance when used for the source of metasurfaces. Consequently, the optical performance of metasurfaces made

L. Liu, F. Zhang, S. Murai, K. Tanaka  
Department of Material Chemistry  
Graduate School of Engineering  
Kyoto University  
Nishikyo-ku, Kyoto 615-8510, Japan  
E-mail: [murai@dipole7.kuic.kyoto-u.ac.jp](mailto:murai@dipole7.kuic.kyoto-u.ac.jp)

 The ORCID identification number(s) for the author(s) of this article can be found under <https://doi.org/10.1002/adpr.202100235>.

© 2021 The Authors. Advanced Photonics Research published by Wiley-VCH GmbH. This is an open access article under the terms of the Creative Commons Attribution License, which permits use, distribution and reproduction in any medium, provided the original work is properly cited.

DOI: 10.1002/adpr.202100235

from sputtered/electron beam-deposited Si is not high in most cases.

Here we demonstrate a robust way of improving the optical performance of sputter-originated Si metasurfaces by postheating using the rapid thermal annealing (RTA) technique. Extrinsic optical losses in nanophotonics come from microscopic disorders of crystal structures, that is, defects<sup>[12–16]</sup> and macroscopic surface roughness of the nanostructures.<sup>[17–19]</sup> One way of reducing the losses of metasurfaces is to start from high-quality thin films<sup>[20]</sup> for fabrication. However, the microscopic defects and/or macroscopic surface roughness can be introduced during the nanofabrication process. It is noted that RTA is applicable to the metasurfaces fabricated from thin films of any quality. RTA has been reported to be an effective way to improve the optical performance of nanostructures through the reduction of the number of defects.<sup>[21,22]</sup> For metallic NPs, the blueshifted plasmon frequency and reduced damping factor in the Drude–Lorentz-type dielectric function lead to the blueshifted and narrowed plasmonic resonances after RTA.<sup>[12,14,16]</sup> For Si, RTA is known to be effective for crystallization of amorphous films,<sup>[23]</sup> but the application to metasurfaces is very limited.<sup>[15]</sup> In this report, we experimentally show that the RTA can refine the sputter-made *a*-Si so as to retain the optical constants close to *c*-Si. With the capability of optical constant refinement by RTA, we design and experimentally demonstrate that the sputter-originated Si metasurface shows the lattice Kerker effect. The Si

nanodisk array after RTA sustains sharp SLRs with ED and MD, which cross at a specific angle defined by lattice periodicity. At the crossing condition, the near-zero reflectance and near-perfect absorptance due to lattice Kerker effect appear. We further demonstrate a highly directional photoluminescence (PL) from the thin emitter layer deposited on the metasurface by making use of the reciprocal process of near-zero reflectance: The PL shows a distinct peak in the forward direction, while it is reduced in the backward direction at the lattice Kerker condition. The finite-difference time domain (FDTD) method and the multipole expansion are used to give the physical interpretation.

## 2. Results and Discussion

### 2.1. Optical Dispersion Before and After RTA

The designed metasurface comprises the *a*-Si nanodisks with a diameter of 270 nm and a height of 90 nm, arranged in a square lattice with a period of 340 nm (see Section 1, Supporting Information, for the fabrication details). The periodic arrangement induces SLRs coupling the local Mie resonances, both ED and MD, through diffraction orders. Polarized illumination enables selective excitation of ED-/MD-coupled SLRs, and dispersive nature of the SLRs enables the fine tuning of the spectral overlap between them.<sup>[15]</sup> The fabricated Si nanodisk array, shown in **Figure 1a**, confirms the as-designed array geometries,

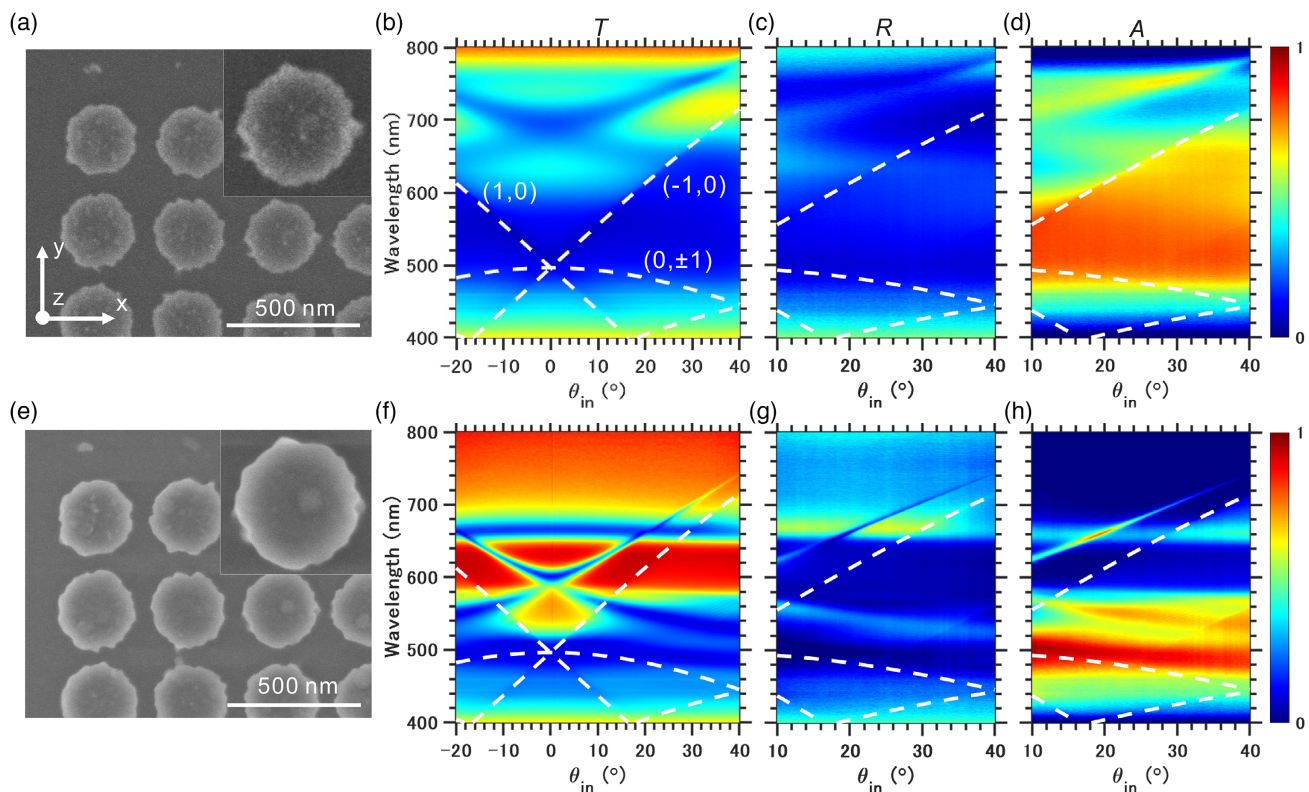


**Figure 1.** Top-View SEM images of Si nanodisk array a) before and e) after RTA. Experimental b,f) transmittance (*T*), c,g) reflectance (*R*), and d,h) absorptance (*A*) spectrum of the Si nanodisk arrays before/after the RTA for TM-polarized light, that is, the electric field oscillating along the *x*-direction, as a function of  $\theta_{in}$  defined in the *z* – *x* plane. The plot ranges of *R* and *A* are limited to  $\theta_{in} \geq 10^\circ$  due to the working range of the rotation stage. The white dashed lines denote the diffraction orders.

but the nanodisks possess rough sidewalls and some pimples on the surface.

We measured the zeroth-order transmission by a collimated and polarized beam, where the nanodisk arrays were immersed in index-matching oil ( $n = 1.46$ ) to provide an optically homogeneous environment. The measurement was conducted using a home-built rotation stage setup (see the sketch in Figure S1a, Supporting Information). The transmission spectra of the as-made *a*-Si metasurface for TM-polarized light, where the electric field is polarized along the  $x$ -axis (see the inset of SEM images in Figure 1 for the coordinate), are shown in Figure 1b as a function of the angle of incidence ( $\theta_{\text{in}}$ ). Three dips appear at  $\lambda = 500, 688,$  and  $765$  nm at  $\theta_{\text{in}} = 0^\circ$ . Also plotted as the white dashed lines are the Rayleigh anomalies, satisfying

$$k_0 = k_x(\theta_{\text{in}}) \pm G(m_1, m_2) \quad (1)$$

where  $k_0$  is the wavevector of the in-plane diffracted orders,  $k_x$  is the in-plane component of the incident wavevector, which depends on the incident angle  $\theta_{\text{in}}$ , and  $G(m_1, m_2) = (2\pi/a)(m_1\vec{x} + m_2\vec{y})$  is the reciprocal lattice vector with  $m_1$  and  $m_2$  defining the diffraction orders in the  $x$ - and  $y$ -directions, respectively. As  $\theta_{\text{in}}$  deviates from  $0^\circ$ , the dip at  $\lambda = 688$  nm splits and follows the dispersions of  $(m_1, m_2) = (\pm 1, 0)$  and  $(0, \pm 1)$  diffraction orders. Under TM illumination, the EDs along the  $x$ -axis ( $\text{ED}_x$ ) are excited in each disk, which preferentially couple to  $(0, \pm 1)$  orders.<sup>[10]</sup> Meanwhile the MDs along the  $y$ -axis ( $\text{MD}_y$ ) couple to  $(\pm 1, 0)$  orders. The split of the mode at  $\lambda = 688$  nm following  $(\pm 1, 0)$  and  $(0, \pm 1)$  means that it consists of both  $\text{ED}_x$  and  $\text{MD}_y$  components. Meanwhile, the dip at  $\lambda = 765$  nm and  $\theta_{\text{in}} = 0^\circ$  is almost dispersionless, indicating this mode consists of  $\text{ED}_x$ . Interestingly, this  $\text{ED}_x$  mode at  $\lambda = 765$  nm crosses the dispersive  $\text{MD}_y$  mode at around  $\theta_{\text{in}} = 20^\circ$ , as shown in Figure 1. We revisit the origin of the mode later using the multipole expansion analysis.

We further examine the optical properties by measuring reflectance ( $R$ ) and absorptance ( $A = 1 - T - R$ ) around the crossing region (Figure 1c,d). A reflectance/absorptance feature appears along the SLRs. Nevertheless, the resonances are so broad that the Kerker effect is not obvious, which is due to the large loss of the *a*-Si nanodisks. The metasurface also shows a broad and featureless resonance below  $\lambda = 600$  nm, which is affected by ED and higher-order modes, and we will not focus on them in this work.

After the RTA treatment (at  $1000^\circ\text{C}$  for 20 min in  $\text{H}_2$  (3 vol%) /Ar), the sidewalls of the nanodisks are slightly smoothed (see scanning electron microscope (SEM) image in Figure 1e), which could reduce the radiation loss.<sup>[19]</sup> A zoom-up image on the single nanodisk in the inset indicates that the diameter of nanodisk is slightly increased, which will be investigated in the following subsection. The RTA brings a drastic change in optical transmission, as shown in Figure 1f. The resonances are entirely blueshifted with the increase in background transmission. Both the MD- and ED-SLRs are more distinct and appear as narrow resonant peaks at normal incidence at  $\lambda = 600$  and  $666$  nm with the minimum transmittance of 13% and 18%, respectively. In the reflectance spectra (Figure 1g), ED-SLR shows high reflectance, while MD-SLR is less reflective, and the crossing region appears as a line with low reflectance.

In the absorptance map (Figure 1h), the MD-SLR and the dispersionless  $\text{ED}_x$  cross at  $\lambda = 666$  nm and  $\theta_{\text{in}} = 20^\circ$ , where the absorptance hits the maximum around 0.77 while the reflectance is minimal. This indicates that the constructive interference of the two mode increases the absorptance and suppresses the reflectance.

As for TE polarization, the results are summarized in Figure S1, Supporting Information. The radiation of the scattered field of  $\text{ED}_y$  is maximum in the  $x$ -direction, coupling preferentially to the  $(\pm 1, 0)$  diffraction orders as the incident angle is changed in the  $z - x$  plane. After the RTA, the dispersive feature of ED-SLRs due to this coupling is observed in Figure S1e, Supporting Information, while  $\text{MD}_x$  couples to the  $(0, \pm 1)$  diffraction orders and shows nondispersive MD-SLRs at  $\lambda \approx 600$  nm. At an oblique incidence, the symmetry-protected bound state in the continuum (BIC) mode emerging from  $\text{MD}_z$  becomes leaky mode and appears at  $\lambda \approx 760$  nm.<sup>[15]</sup>

## 2.2. RTA-Induced Crystallization

The crystallization of *a*-Si is obvious from the cross-sectional transmission electron microscope (TEM) analysis (Figure 2a,c). The emergence of the polycrystalline phase is evidenced by the fast Fourier transfer analysis on the TEM images, as shown in Figure 2b,d. The surface roughness is also examined by atomic force microscope, showing that the surface is slightly smoothed after RTA (see Figure S2, Supporting Information). The nanodisk was identified as polycrystalline Si and covered by a uniform oxide layer. We confirm that the surface is indeed oxidized by removing the surface oxide layer by immersing it in an aqueous hydrofluoric (HF) acid solution. The transmittance in an immersion oil ( $n = 1.46$ ) is nearly unchanged after the HF treatment, even though the SEM image clearly shows the shrinkage of the diameter (see Figure S3c,d, Supporting Information). The crystallization of *a*-Si after RTA is detected by X-ray diffraction (XRD) and Raman spectroscopy for the thin film (see Figure S4, Supporting Information), which confirms the internal structural changes brought up by RTA. After RTA, the sharp XRD peaks appear on the single broad halo pattern from the glass substrate, and the clearly narrowed Raman peak around  $520\text{ cm}^{-1}$  proves the improved crystallinity of Si.

We determine the refractive index  $n$  and extinction coefficient  $k$  of *a*-Si before and after RTA by spectroscopic ellipsometry of the thin film. As presented in Figure S5, Supporting Information, the data are compared with the representative references of *c*-Si,<sup>[24]</sup> *a*-Si,<sup>[25]</sup> and *a*-Si:H.<sup>[26]</sup> The dielectric function changes drastically by the RTA treatment:  $n$  of *a*-Si approaches that of *c*-Si because of crystallization. Before RTA, *a*-Si has a pronounced  $k$  due to the disorder-induced broadening of its bands<sup>[27]</sup> and greatly reduced  $k$  is observed for the RTA-treated *a*-Si, which indicates the decreased number of defects and appearance of the crystalline phase in *a*-Si. It is noted that the  $n$  and  $k$  of the sputter-made thin film after RTA are comparable with those of the polycrystalline Si deposited by CVD. The RTA allows to obtain high-quality Si films while avoiding the use of toxic  $\text{SiH}_4$  gas. We also examined the effects of the temperature and time of RTA, as summarized in Figure S6, Supporting Information.

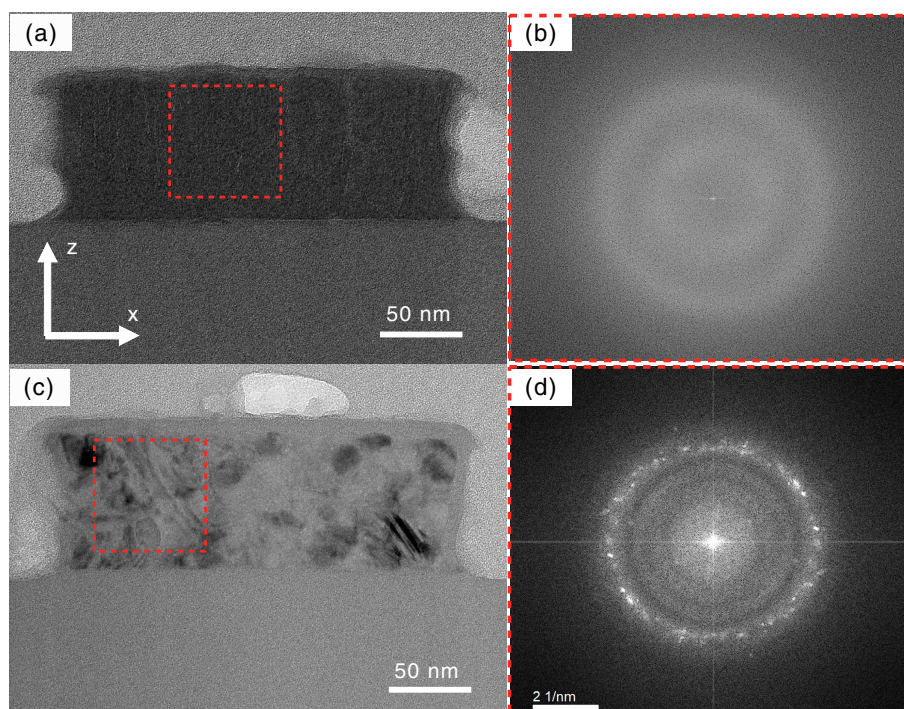


**Figure 2.** Cross-sectional TEM images of the sample a) before and c) after RTA. The corresponding FFT diffraction patterns b) before and d) after RTA from the red dotted boxes in (a) and (c).

The ellipsometry measurement also clarifies that the film becomes thinner after treatment, which indicates the increase in the density of the film. The sputter-made film is amorphous and the Si atoms are packed less densely than the crystalline Si, and heat treatment densifies the packing by removing the possible inside voids. It is also confirmed that the film is coated with a thin ( $\approx 10$  nm) layer of silicon oxide, as often observed especially after high-temperature treatment.<sup>[28–30]</sup>

### 2.3. Numerical Simulations

The experimental features, including the emergence of the lattice Kerker effect after RTA, can be well reproduced by the FDTD simulation. We extract the geometry of the nanodisk from the TEM images. In the simulations, the Si core of the nanodisk after (before) RTA was defined as upper diameter = 282 (280) nm, bottom diameter = 244 (248) nm, and height = 85 (90) nm. Note that the surface oxide layer (around 10 nm) has a similar refractive index with the homogeneous background of  $n = 1.46$ ; thus, we ignore its effect in the simulation. The dispersive values of  $n$  and  $k$  of Si before and after RTA are adopted by our experimental results (Figure S5, Supporting Information). We also ignore the surface roughness of the nanodisks.

The corresponding simulated results for TM polarization displayed in **Figure 3** are in excellent agreement with the experimental results in Figure 1. For the as-made *a*-Si metasurface (Figure 3a–c), the broad features appear in transmittance/reflectance/absorptance maps. Their drastic changes by RTA are clearly reproduced. This indicates that the change of optical constants accompanying the crystallization is the main reason for

the drastic change in optical response. At  $\theta_{\text{in}} = 22^\circ$ , where the MD- and ED-SLRs overlap, near-zero reflectance, or near-zero backscattering, is observed, because the first Kerker condition is satisfied. However, the refined *a*-Si arrays still shows a small but finite loss at this wavelength, leading to the near-perfect absorptance of 90% at  $\theta_{\text{in}} = 22^\circ$  (see Figure 3f) in simulation and 77% in experiment. We note that the imperfect fabrication of the nanostructures (see Figure 1a,e) causes additional scattering losses, which are indeed responsible for the discrepancy between experiment and simulation, including the slight mismatch in the angle of near-zero reflectance/near-perfect absorptance, that is,  $\theta_{\text{in}} = 20^\circ$  and  $22^\circ$  for the experiment and simulation, respectively.<sup>[19]</sup>

For the sake of completeness, we also perform the simulation for TE polarization, both before and after the RTA. The results, summarized in Figure S7, Supporting Information, show that the agreement between the simulation and the experiments is also excellent.

### 2.4. Lattice Kerker Condition

In periodic lattices, we can control ED- and MD-SLRs independently and bring them into overlap by tuning the array dimensions<sup>[11]</sup> and/or the angle of incidence.<sup>[31,32]</sup> In the present work, oblique incidence of TM polarization changes the spectral position of MD-SLR; thus, the MD-SLR and ED-SLR interfere at  $\theta_{\text{in}} = 20^\circ$  at  $\lambda = 666$  nm, where the lattice Kerker effect is achieved after RTA. The lattice Kerker effect appears as the sharp dip in transmittance (**Figure 4a**) and reflectance (Figure 4b) and the peak in absorptance (Figure 4c). Precisely speaking, the

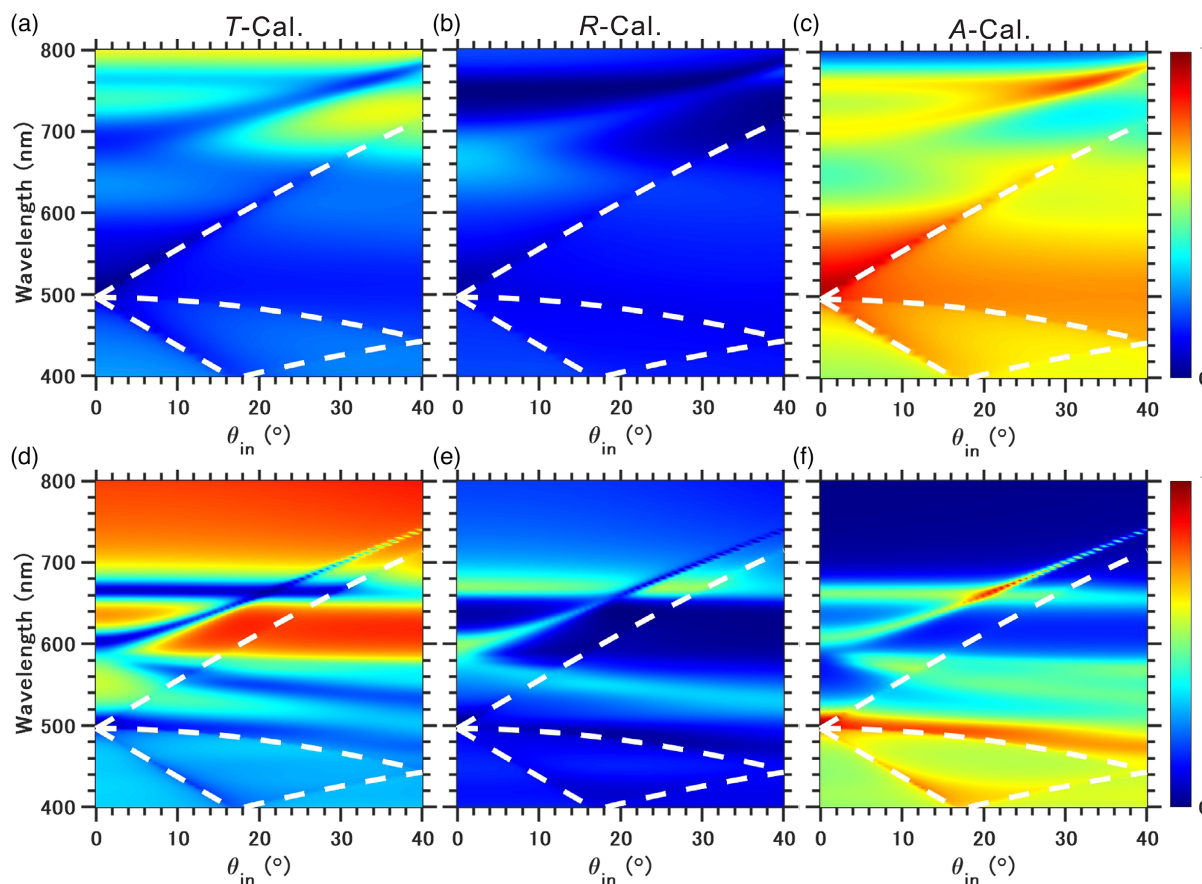


**Figure 3.** Calculated a,d) transmittance (*T-Cal.*), b,e) reflectance (*R-Cal.*), and c,f) absorptance (*A-Cal.*) spectrum of the Si nanodisk arrays before/after the RTA for TM-polarized light as a function of  $\theta_{in}$ . The white dashed lines denote the diffraction orders.

absorptance is not unity and reflectance slightly remains. This is due to the unequal magnitudes of MD and ED, as will be examined for the single nanodisk analysis. The electric field distributions at  $\lambda = 666$  nm in the  $z-x$  and  $y-z$  planes shown in Figure 4d further confirm that light energy is highly confined around and inside the Si nanodisk. The magnetic field is highly confined inside the nanodisk, leading to the near-perfect absorptance at this condition.<sup>[33]</sup>

Perfect absorbers have gained great attention in recent years, because of their potential applications in optoelectronics such as sensors, thermal emitters, solar cells, and thermophotovoltaics.<sup>[33–36]</sup> Most widely studied perfect absorbers comprise multiple-layer structures, including dielectric/metallic resonators on back reflectors,<sup>[37,38]</sup> metal–insulator–metal,<sup>[39–44]</sup> and multilayer Fabry–Perot cavity structures.<sup>[45]</sup> Alternatively, single-layer dielectric periodic arrays can achieve perfect absorption with much simpler geometries, utilizing the Kerker effect with finite absorption by each nanodisk. The relevant researches have been emphasized in GHz,<sup>[46]</sup> THz,<sup>[47–50]</sup> and infrared,<sup>[51]</sup> while single-layer dielectric perfect absorbers in the visible region is limited. Moreover, many of the preceding works in the near-infrared and visible regions employ *a*-Si<sup>[33]</sup> and *a*-Ge<sup>[51]</sup> to absorb light, wherein the photocarrier generation is less effective compared with the crystalline counterparts. Our metasurface,

comprising *c*-Si after RTA, shows the narrow near-perfect absorptance in the visible region (at  $\lambda = 666$  nm with full width at half maximum = 10.9 nm), manifesting the comparable characters to the preceding absorbers. This feature is useful for filters and/or detectors that cut and/or pick up signals coming from the specific angle.

## 2.5. Directional Emission Associated with the Lattice Kerker Effect

The coupling of PL with Kerker effect and related bound states in the continuum (BIC) can bring about an anisotropic emission that breaks out-of-plane symmetry.<sup>[52–58]</sup> We elucidate the metasurface-induced modulation of PL by depositing a thin light-emitting layer on top of the metasurface (see Section 1, Supporting Information, for the deposition process and the layer composition). The sample was excited by a blue laser ( $\lambda = 440.6$  nm) and the emission was collected by a detector rotating around the sample so as to measure the spectra as a function of emission angle ( $\theta_{em}$ ) defined in the  $z-x$  plane (see the sketch in the inset of Figure 5a for the experimental configuration). The enhancement is defined as the emission intensity divided by that from the emitter layer on an unstructured silica glass substrate, which is the reference. The PL enhancement for the as-made *a*-Si

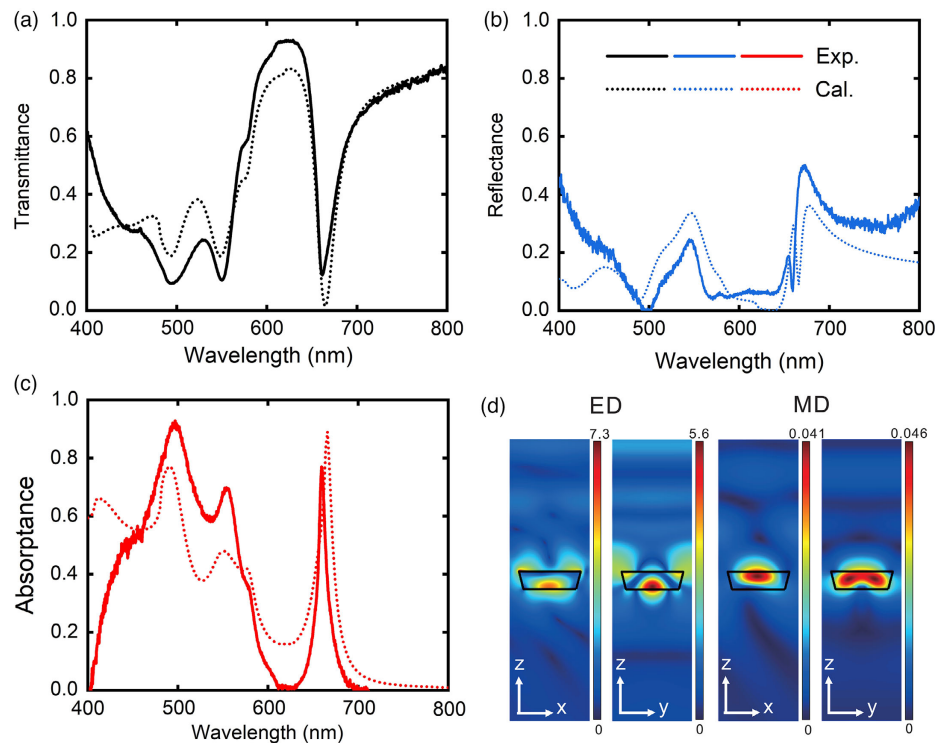


**Figure 4.** Optical response at the lattice Kerker condition for the Si nanodisk array after RTA. Experimental and calculated data at  $\theta_{in} = 20^\circ$  and  $22^\circ$  are plotted as solid and dotted lines respectively for a) transmittance, b) reflectance, and c) absorbance. d) Calculated spatial distributions of the electric and magnetic fields upon illumination at  $\lambda = 666$  nm with  $\theta_{in} = 22^\circ$ .

metasurface is very low in the entire range of  $\theta_{em}$ , as described in Figure S8, Supporting Information, together with the absorption and PL spectra of the reference.

In contrast, the notable features appear in the after-RTA sample (Figure 5a). For this measurement, we used the metasurface with a slightly smaller disk diameter than examined in the previous sections, so that the lattice Kerker condition blueshifted to  $\lambda = 650$  nm at  $\theta_{in} = 25^\circ$  and showed a better overlap with the PL spectrum of the emitter layer. In the colormap in Figure 5a where the PL enhancement is plotted in a range of  $-10^\circ \leq \theta_{em} \leq 190^\circ$ , the broad and dispersionless line appears along the ED-SLR ( $\lambda \approx 650$  nm), while the sharp and dispersive lines of PL enhancement emerge along the MD-SLRs. These enhancements come from the outcoupling effect,<sup>[59]</sup> where the PL from the emitter layer is scattered out via coupling with MD- and ED-SLRs. The dispersion relations of the ED- and MD-SLR are the same at both sides of the sample, and thus the PL enhancement is symmetric with respect to the data at  $\theta_{in} = 90^\circ$ . However, a difference is found at the lattice Kerker condition where the ED and MD cross: the PL is relatively weakened at the lattice Kerker condition at  $\theta_{em} = 25^\circ$ , while it is enhanced at  $155^\circ$ . The polar plot in the inset showing the PL enhancement at  $\lambda = 653$  nm further visualizes this anisotropic emission. Given the experimental geometry as depicted in the inset, the PL coupled to the backward scattering by the metasurface is detected at  $\theta_{em} \leq 90^\circ$ , while that coupled to the forward scattering  $\theta_{em} \geq 90^\circ$ . The decrease and increase in PL intensity at  $\theta_{in} = 25^\circ$  and  $155^\circ$  are the consequences of the lattice Kerker effect. These modulations of the PL are

better compared by the cuts at the lattice Kerker condition in Figure 5c. In the backward direction, the destructive interference of the MD and ED cancels PL emission at  $\lambda \approx 650$  nm, while the constructive interference in the forward direction leads to the PL enhancement at this wavelength.

For the TE component (Figure S9, Supporting Information), the PL enhancement is larger after RTA, as is the case for TM component. The enhancement is up to 6 times though, because of the absence of lattice Kerker effect for TE component.

The PL decay can also characterize this refinement. The change in the PL decay could come from the change in radiative and/or nonradiative decay rates illustrated by the Purcell effect.<sup>[60]</sup> The PL decay curves of the emitter layer on *a*-Si nanodisk arrays before and after RTA treatment (see Figure S10, Supporting Information) show that the influence of RTA on the decay rate is small. Compared with the PL lifetime of the emitter layer on an unstructured glass ( $\tau = 5.54$  ns), the drop in lifetime for the layer on the metasurface before ( $\tau = 4.77$  ns) and after ( $\tau = 4.89$  ns) RTA is less than 15%. This indicates that the Purcell effect is still small in the present metasurfaces.

## 2.6. Optical Response of the Individual Nanodisk

### 2.6.1. Optical Cross Sections

We can take a glance at the optical response of the whole arrays by investigating the scattering behaviors of an individual

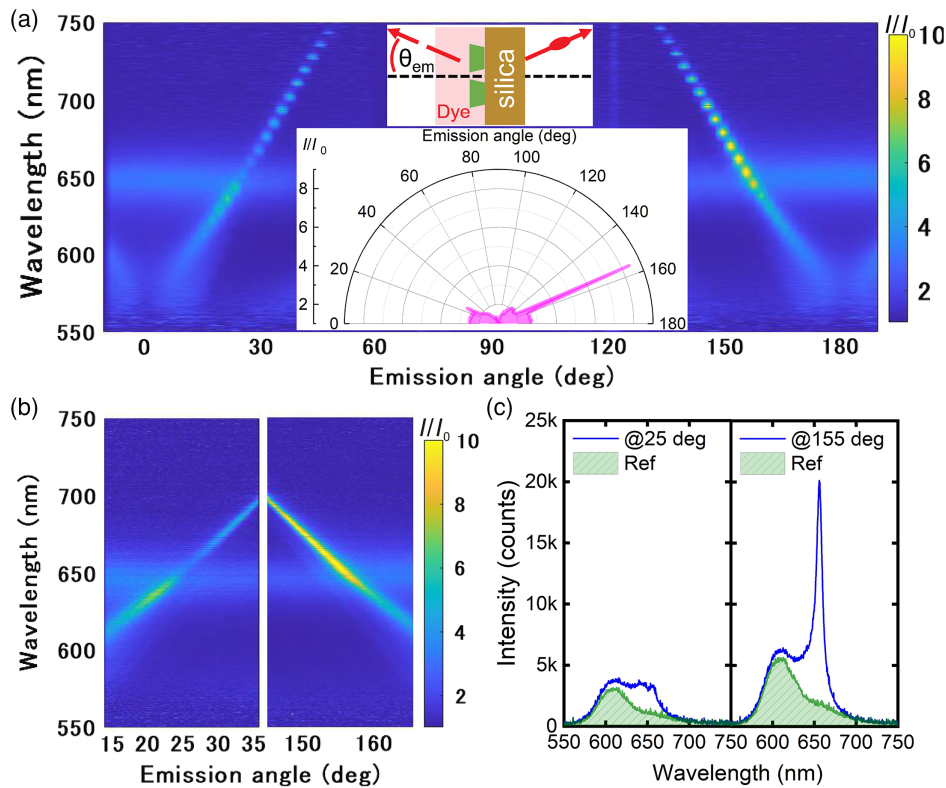


**Figure 5.** a) PL enhancement spectrum for TM-polarized light as a function of  $\theta_{em}$  ( $-10^\circ \sim 190^\circ$ ) for the Si nanodisk arrays after the RTA treatment. As an emitter to couple with the metasurface, a polymethyl methacrylate (PMMA) layer containing 9 wt% lumogen F red 305 (thickness:  $\approx 80$  nm) was deposited on the Si nanodisk array. The sample was excited by a blue laser at a fixed incident angle  $\theta_{in} = 60^\circ$  at the substrate side. The PL enhancement is defined as the emission intensity divided by that from the emitter layer on an unstructured silica glass substrate, which is the reference. The top inset shows the sketch of the experimental geometry. The bottom inset picks up the PL enhancement at  $\lambda = 653$  nm as a function of  $\theta_{em}$ . b) The details for PL enhancement spectrum around the lattice Kerker conditions between  $14^\circ \sim 36^\circ$  and  $144^\circ \sim 166^\circ$  with a step of  $\theta_{em} = 0.3^\circ$ . c) The comparison of PL spectra between backward and forward emission extracted at the  $\theta_{em}$  of  $25^\circ$  and  $155^\circ$ , respectively. PL spectra of the reference are also shown.

nanodisk. The total scattering and absorption cross sections of a single Si nanodisk, both before and after RTA, are depicted in **Figure 6a**. The total scattering cross section (solid curves) varies significantly, where the main dip at  $\lambda = 752$  nm (black) for the as-made disk blueshifts to 640 nm (red) after the RTA treatment. Absorption cross section, represented as the dashed curves, decreases after RTA in the entire range of calculation. The decrease is remarkable especially at longer wavelengths, where SLRs appear in the array. This explains the appearance of sharp and distinct features after RTA. The radiation patterns at the main peaks and dips are plotted in **Figure 6b**: The lightwaves with respective wavelengths are incident on the top side at  $\theta_{in} = 0^\circ$ , and the scattering profile is presented as a 3D polar plot. Note that the scattering field at  $\lambda = 640$  nm, the dip of scattering cross section after RTA, presents the smallest and the forward scattering dominates (**Figure 6b**).

### 2.6.2. Exact Multipole Expansion

To better understand the scattering performances of an individual Si nanodisk, we calculate the scattering cross section as summations of the electromagnetic multipoles contributions, based on the work of Alaei et al.,<sup>[61–63]</sup> The induced multipole moments

are computed using the equations expressed by the induced electric current density.

$$J_\omega(r) = i\omega\epsilon_0(\epsilon_r - \epsilon_d)E_\omega(r) \quad (2)$$

where  $E_\omega(r)$  is the local electric field distribution,  $\epsilon_0$  is the permittivity of free space, and  $\epsilon_r$  is the relative permittivity of the Si obtained by the experimental measurement (see **Figure S5c,d**, Supporting Information). We assume  $\epsilon_d = 1.46^2$  as the homogeneous surrounding medium. For high-refractive-index materials, higher-order modes have negligible contribution to the scattering, and hence, in this work, only ED, MD, electric-, and magnetic-quadrupole (EQ and MQ) have been considered for the sake of simplicity. **Figure 6c,d** shows the multipole contributions to the total scattering cross section of individual Si nanodisk. While the total scattering cross sections in **Figure 6a** are calculated by integrating the energy flux around the Si nanodisk, they agree well with the results from mode decomposition in **Figure 6d**, suggesting a very decent approximation as the contributions from higher-order modes are negligible.

Three peaks appear in the total scattering spectrum after RTA in **Figure 6d**, with the first weaker peak at  $\lambda = 448$  nm and the second peak at 575 nm, as a combined contribution from ED,



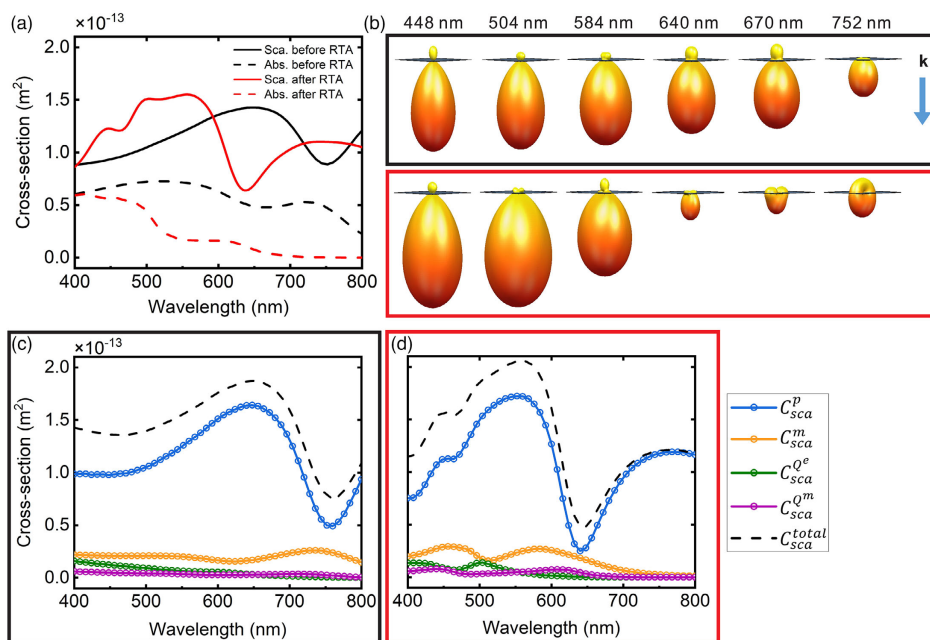


**Figure 6.** a) Total scattering (Sca.) and absorption (Abs.) cross sections and b) radiation patterns of the single nanodisk calculated for before RTA (black box) and after RTA (red box). The plane divides the radiation space into forward and backward direction, and the incident wavevector  $k$  is indicated on the right. Multipole modes of expansion of the total scattering spectra of an individual Si nanodisk c) before RTA (black box) and d) after RTA (red box): ED (blue circles),  $C_{sca}^p$ ; MD (yellow circles),  $C_{sca}^m$ ; electric quadrupole (green circles),  $C_{sca}^e$ ; magnetic quadrupole (purple circles),  $C_{sca}^m$ ; and total scattering spectrum,  $C_{sca}^{total}$  (dark dot line).

MD, EQ, and MQ, while the other peak at 750 nm is from ED. Note this ED term includes a common ED and the higher-order responses, a toroidal dipole (TD).<sup>[63,64]</sup> The scattering dip at around 640 nm can be ascribed to the partial destructive interference between the ED and TD, which suppresses the total ED (ED + TD) contribution in the scattering cross section, that is, close to the anapole excitation condition.<sup>[65]</sup> Furthermore, the magnitude of MD nearly matches with ED at  $\lambda = 640$  nm, offering the possibility to suppress the backward scattering through their interference when they overlap, as illustrated in Figure 6b. Indeed, the fine tuning of the spectral positions of ED and MD via SLR brings the lattice Kerker condition as observed in the array.

### 3. Conclusion

We verify the drastic improvement of optical performance of sputter-made Si metasurfaces by a simple heat treatment. The dielectric function of *a*-Si approaches that of poly-Si after RTA, accompanying the crystallization. Consequently, a narrow-band near-zero reflectance and near-perfect absorptance (with a  $Q$ -factor  $\approx 60$ ) due to the lattice Kerker effect, which is hidden in the as-made *a*-Si metasurface, emerges after RTA. Multipole analysis for the single-Si nanodisk confirms that the magnitude of ED is decreased by the interaction with TD to be similar to that of MD around the Kerker condition. Further, we achieve anisotropic radiation of PL into the forward direction at the lattice Kerker condition. The set of sputter-made *a*-Si metasurfaces and the conversion into *c*-Si via postannealing is a robust and

powerful way of preparing high-optical-performance Si-based metasurfaces and have significant potential applications in thin and efficient optical components including filters, detectors, and reflectors.

### Supporting Information

Supporting Information is available from the Wiley Online Library or from the author.

### Acknowledgements

L.L. and F.Z. equally contributed to this work. This work was partly supported by the Nanotechnology Hub, Kyoto University (JPMXP09F19NMC042). The authors gratefully acknowledge the financial support by Kakenhi (19K22058, 19H02434, and 21H04619) from MEXT, Japan and the Asahi Glass Foundation.

### Conflict of Interest

The authors declare no conflict of interest.

### Data Availability Statement

The data that support the findings of this study are available from the corresponding author upon reasonable request.

## Keywords

anisotropic photoluminescence, Kerker conditions, multipole expansion analyses, rapid thermal annealing, surface lattice resonances

Received: September 28, 2021

Revised: November 21, 2021

Published online: December 22, 2021

- [1] S. Enoch, N. Bonod, *Plasmonics: From Basics to Advanced Topics*, vol. 167, Springer, Berlin **2012**.
- [2] J. B. Khurgin, *Nat. Nanotechnol.* **2015**, 10, 2.
- [3] A. I. Kuznetsov, A. E. Miroshnichenko, M. L. Brongersma, Y. S. Kivshar, B. Luk'yanchuk, *Science* **2016**, 354, aag2472.
- [4] I. Staude, J. Schilling, *Nat. Photonics* **2017**, 11, 274.
- [5] K. Koshelev, Y. Kivshar, *ACS Photonics* **2021**, 8, 102.
- [6] S. Jahani, Z. Jacob, *Nat. Nanotechnol.* **2016**, 11, 23.
- [7] M. Kerker, D. S. Wang, C. L. Giles, *J. Opt. Soc. Am.* **1983**, 73, 765.
- [8] W. Liu, Y. S. Kivshar, *Opt. Express* **2018**, 26, 13085.
- [9] W. Liu, Y. S. Kivshar, *Philos. Trans. R. Soc. A* **2017**, 375, 20160317.
- [10] S. Murai, G. W. Gabriel, W. Castellanos, T. Raziman, A. G. Curto, J. Gómez Rivas, *Adv. Opt. Mater.* **2020**, 8, 1902024.
- [11] V. E. Babicheva, A. B. Evlyukhin, *Laser Photonics Rev.* **2017**, 11, 1700132.
- [12] A. B. Dahlin, T. Sannomiya, R. Zahn, G. A. Sotiriou, J. Voros, *Nano Lett.* **2011**, 11, 1337.
- [13] M. Bosman, L. Zhang, H. Duan, S. F. Tan, C. A. Nijhuis, C.-W. Qiu, J. K. Yang, *Sci. Rep.* **2014**, 4, 1.
- [14] F. Zhang, J. Proust, D. Gérard, J. Plain, J. Martin, *J. Phys. Chem. C* **2017**, 121, 7429.
- [15] S. Murai, D. R. Abujetas, G. W. Castellanos, J. A. Sánchez-Gil, F. Zhang, J. G. Rivas, *ACS Photonics* **2020**, 7, 2204.
- [16] M. Higashino, S. Murai, K. Tanaka, *J. Phys. Chem. C* **2020**, 124, 27687.
- [17] J. Rodríguez-Fernández, A. M. Funston, J. Pérez-Juste, R. A. Álvarez-Puebla, L. M. Liz-Marzán, P. Mulvaney, *Phys. Chem. Chem. Phys.* **2009**, 11, 5909.
- [18] Y.-W. Lu, L.-Y. Li, J.-F. Liu, *Sci. Rep.* **2018**, 8, 1.
- [19] F. Zhang, J. Plain, D. Gérard, J. Martin, *Nanoscale* **2021**, 13, 1915.
- [20] Y. Yang, G. Yoon, S. Park, S. D. Namgung, T. Badloe, K. T. Nam, J. Rho, *Adv. Mater.* **2021**, 33, 2005893.
- [21] M.-C. Lee, M. C. Wu, *J. Microelectromech. Syst.* **2006**, 15, 338.
- [22] M. Bosman, L. Zhang, H. Duan, S. F. Tan, C. A. Nijhuis, C.-W. Qiu, J. K. Yang, *Sci. Rep.* **2014**, 4, 1.
- [23] R. Kakkad, J. Smith, W. S. Lau, S. J. Fonash, R. Kerns, *J. Appl. Phys.* **1989**, 65, 2069.
- [24] D. E. Aspnes, A. Studna, *Phys. Rev. B* **1983**, 27, 985.
- [25] D. T. Pierce, W. E. Spicer, *Phys. Rev. B* **1972**, 5, 3017.
- [26] Z. C. Holman, A. Descoedres, L. Barraud, F. Z. Fernandez, J. P. Seif, S. De Wolf, C. Ballif, *IEEE J. Photovoltaics* **2012**, 2, 7.
- [27] G. Cody, T. Tiedje, B. Abeles, B. Brooks, Y. Goldstein, *Phys. Rev. Lett.* **1981**, 47, 1480.
- [28] Y. Nakamine, T. Kodera, K. Uchida, S. Oda, *Jpn. J. Appl. Phys.* **2011**, 50, 115002.
- [29] M. Y. Bashouti, K. Sardashti, J. Ristein, S. H. Christiansen, *Phys. Chem. Chem. Phys.* **2012**, 14, 11877.
- [30] M. Morita, T. Ohmi, E. Hasegawa, M. Kawakami, M. Ohwada, *J. Appl. Phys.* **1990**, 68, 1272.
- [31] V. E. Babicheva, *MRS Commun.* **2018**, 8, 1455.
- [32] A. D. Utyushev, V. I. Zakomirnyi, A. E. Ershov, V. S. Gerasimov, S. V. Karpov, I. L. Rasskazov, in *Photonics*, vol. 7, Multidisciplinary Digital Publishing Institute, Basel **2020**, p. 24.
- [33] C.-Y. Yang, J.-H. Yang, Z.-Y. Yang, Z.-X. Zhou, M.-G. Sun, V. E. Babicheva, K.-P. Chen, *ACS Photonics* **2018**, 5, 2596.
- [34] Y. Ra'Di, C. Simovski, S. Tretyakov, *Phys. Rev. Appl.* **2015**, 3, 037001.
- [35] T. D. Dao, K. Chen, S. Ishii, A. Ohi, T. Nabatame, M. Kitajima, T. Nagao, *ACS Photonics* **2015**, 2, 964.
- [36] R. Xu, J. Takahara, *Opt. Lett.* **2021**, 46, 805.
- [37] A. A. Rifat, M. Rahmani, L. Xu, A. E. Miroshnichenko, *Materials* **2018**, 11, 1091.
- [38] Y. Cheng, C. Du, *Opt. Mater.* **2019**, 98, 109441.
- [39] K. Aydin, V. E. Ferry, R. M. Briggs, H. A. Atwater, *Nat. Commun.* **2011**, 2, 517.
- [40] P. C. Wu, C. Y. Liao, J. W. Chen, D. P. Tsai, *Adv. Opt. Mater.* **2017**, 5, 1600581.
- [41] N. Liu, M. Mesch, T. Weiss, M. Hentschel, H. Giessen, *Nano Lett.* **2010**, 10, 2342.
- [42] W. Wang, Y. Qu, K. Du, S. Bai, J. Tian, M. Pan, H. Ye, M. Qiu, Q. Li, *Appl. Phys. Lett.* **2017**, 110, 101101.
- [43] Y. Qu, Q. Li, K. Du, L. Cai, J. Lu, M. Qiu, *Laser Photonics Rev.* **2017**, 11, 1700091.
- [44] Y. Chen, X. Li, X. Luo, S. A. Maier, M. Hong, *Photonics Res.* **2015**, 3, 54.
- [45] C.-S. Park, S.-S. Lee, *Sci. Rep.* **2020**, 10, 17727.
- [46] J. Y. Suen, K. Fan, W. J. Padilla, *Adv. Opt. Mater.* **2019**, 7, 1801632.
- [47] K. Fan, J. Y. Suen, X. Liu, W. J. Padilla, *Optica* **2017**, 4, 601.
- [48] X. Ming, X. Liu, L. Sun, W. J. Padilla, *Opt. Express* **2017**, 25, 24658.
- [49] X. Liu, K. Fan, I. V. Shadrivov, W. J. Padilla, *Opt. Express* **2017**, 25, 191.
- [50] K. Fan, I. V. Shadrivov, A. E. Miroshnichenko, W. J. Padilla, *Opt. Express* **2021**, 29, 10518.
- [51] J. Tian, H. Luo, Q. Li, X. Pei, K. Du, M. Qiu, *Laser Photonics Rev.* **2018**, 12, 1800076.
- [52] S. R. K. Rodriguez, F. B. Arango, T. P. Steinbusch, M. A. Verschuuren, A. F. Koenderink, J. G. Rivas, *Phys. Rev. Lett.* **2014**, 113, 247401.
- [53] I. M. Hancu, A. G. Curto, M. Castro-López, M. Kuttge, N. F. van Hulst, *Nano Lett.* **2014**, 14, 166.
- [54] A. F. Cihan, A. G. Curto, S. Raza, P. G. Kik, M. L. Brongersma, *Nat. Photonics* **2018**, 12, 284.
- [55] S. I. Azzam, K. Chaudhuri, A. Lagutchev, Z. Jacob, Y. L. Kim, V. M. Shalaev, A. Boltasseva, A. V. Kildishev, *Laser Photonics Rev.* **2021**, 15, 2000411.
- [56] J.-H. Yang, Z.-T. Huang, D. N. Maksimov, P. S. Pankin, I. V. Timofeev, K.-B. Hong, H. Li, J.-W. Chen, C.-Y. Hsu, Y.-Y. Liu, T.-C. Lu, T.-R. Lin, C.-S. Yang, K.-P. Chen, *Laser Photonics Rev.* **2021**, 15, 2100118.
- [57] M. Wu, S. T. Ha, S. Shendre, E. G. Durmusoglu, W.-K. Koh, D. R. Abujetas, J. A. Sánchez-Gil, R. Paniagua-Domínguez, H. V. Demir, A. I. Kuznetsov, *Nano Lett.* **2020**, 20, 6005.
- [58] M.-S. Hwang, H.-C. Lee, K.-H. Kim, K.-Y. Jeong, S.-H. Kwon, K. Koshelev, Y. Kivshar, H.-G. Park, *Nat. Commun.* **2021**, 12, 4135.
- [59] G. Lozano, D. J. Louwers, S. R. Rodriguez, S. Murai, O. T. Jansen, M. A. Verschuuren, J. G. Rivas, *Light: Sci. Appl.* **2013**, 2, 66.
- [60] E. M. Purcell, H. C. Torrey, R. V. Pound, *Phys. Rev.* **1946**, 69, 37.
- [61] R. Alae, C. Rockstuhl, I. Fernandez-Corbaton, *Opt. Commun.* **2018**, 407, 17.
- [62] R. Alae, C. Rockstuhl, I. Fernandez-Corbaton, *Adv. Opt. Mater.* **2019**, 7, 1800783.
- [63] T. Hinamoto, M. Fujii, *OSA Continuum* **2021**, 4, 1640.
- [64] A. B. Evlyukhin, T. Fischer, C. Reinhardt, B. N. Chichkov, *Phys. Rev. B* **2016**, 94, 205434.
- [65] A. E. Miroshnichenko, A. B. Evlyukhin, Y. F. Yu, R. M. Bakker, A. Chipouline, A. I. Kuznetsov, B. Luk'yanchuk, B. N. Chichkov, Y. S. Kivshar, *Nat. Commun.* **2015**, 6, 8069.